

Signal Conditioning Technique for Position Sensitive Photodetectors to Manipulate Pixelated Crystal Identification Capabilities

Frances W. Y. Lau, Arne Vandenbroucke, Paul Reynolds, Holly Ho, Derek Innes, and Craig S. Levin

Abstract—We analyze performance of position sensitive detectors such as Position Sensitive Avalanche Photodiodes (PSAPDs) used to readout pixelated scintillation crystal arrays. Crystal identification abilities are determined by analyzing the flood histogram. A good flood histogram has peaks which are as well separated and as narrow as possible since this enables better crystal identification, and ultimately improves spatial resolution. We present a signal conditioning circuit for the readout of PSAPDs and investigate how the tradeoff between the parameters of the signal conditioning circuit components, the PSAPD bias voltage, and the input dynamic range and noise of the preamplifier influence the flood histogram. The signal conditioning circuit involves adding a resistor and a capacitor between the four spatial channels of the detector and the preamplifier. This technique was verified and studied both experimentally and by simulation using PSAPDs coupled to 8×8 arrays of 1 mm^3 scintillation crystals. Results showed that the flood histogram is not very sensitive to the exact value of the resistor in the signal conditioning circuit, but in general a resistance about twice the sheet resistance of the position sensitive detector is recommended. The capacitor in the signal conditioning circuit should be chosen by taking preamplifier input dynamic range, preamplifier noise, and detector noise into account.

Index Terms—Avalanche photodiode, photodetectors, Positron Emission Tomography, Position Sensitive Particle Detectors, solid scintillation detectors, spatial resolution.

I. INTRODUCTION

POSITION sensitive photodetectors, such as Position Sensitive Avalanche Photodiodes (PSAPDs) [1], [2], Position Sensitive Solid-State Photomultipliers (PS-SSPMs) [3], and Position Sensitive Photomultiplier Tubes (PMTs) [4] can readout a

large number of scintillation crystal pixels with only a few electronics channels. These position-sensitive photodetectors can position interactions using four corner contacts (“spatial channels”) on a resistive sheet on one side of the detector (e.g., anode) by evaluating the position-dependent charge splitting.

Position sensitive photodetectors are often coupled to pixelated scintillation crystals to form a detector module. These detector modules can be characterized by analyzing flood histograms, that is, images produced by flood irradiating the detector module. A good flood histogram has peaks which are as well separated and narrow as possible since this reduces the probability of assigning the wrong crystal to a hit and thus ultimately improves spatial resolution. To achieve this, the minimum requirement is that the detector signals do not saturate since saturation causes the crystals at the edge of the array to be irreversibly inseparable.

Another metric for position sensitive photodetectors is the equivalent noise charge (ENC) or signal to noise ratio (SNR) of the signals measured at its contacts. These parameters can also be predicted by the flood histogram since there is a relationship between the noise of a photodetector and the width of the peaks in the flood histogram [5]. The SNR is also reflected in the energy resolution. However, this relationship is blurred by the limited intrinsic contribution of the scintillation crystal and therefore less indicative of SNR [6].

Position sensitive photodetectors typically produce flood histograms with a pin-cushion shape due to the non-linearity of charge sharing between contacts from the device’s sheet resistance. This distortion can be corrected by post-processing [7], [8]. However, if the shape is severely distorted, corner and edge crystals are not clearly identifiable, and post-processing correction capability is limited.

The properties of the position-sensitive photodetectors, the scintillation crystal, and the electronic circuits used to readout the photodetectors can affect the flood histogram and the SNR. We present a signal conditioning circuit for the readout of PSAPDs and we investigate how the tradeoff between the following parameters influences the flood histogram and SNR: 1) Input dynamic range and noise of electronics, 2) Photodetector bias voltage, and 3) Resistor (R_{spatial}) and capacitor (C_{spatial}) values of the presented signal conditioning circuit.

This work focuses on PSAPDs, a device which other researchers such as [9]–[11] have incorporated into their imaging system designs. However, the basic signal conditioning concepts presented could be helpful to those using PS-SSPMs, APD arrays, or SSPM arrays.

Manuscript received January 20, 2012; revised April 12, 2012 and July 02, 2012; accepted July 10, 2012. Date of publication September 06, 2012; date of current version October 09, 2012. This work was supported in part by R01 CA119056 and R01 CA 119056-S1 (ARRA) from NIH, the California Breast Cancer Research Program 16 GB-0060, Stanford Bio-X Fellowship, Postdoctoral Research Fellowship from DoD BC094158, and ARCS Scholarship.

F. W. Y. Lau, P. Reynolds, and H. Ho are with the Department of Electrical Engineering, Stanford University, Stanford, CA, 94305 USA.

A. Vandenbroucke and D. Innes are with the Department of Radiology, Stanford University, Stanford, CA, 94305 USA.

C. S. Levin is with the Department of Electrical Engineering, Stanford University, Stanford, CA, 94305 USA, with the Department of Radiology, Stanford University, Stanford, CA, 94305 USA, and also with the Departments of Physics and Bioengineering, Stanford University, Stanford, CA, 94305 USA (e-mail: cslevin@stanford.edu).

Color versions of one or more of the figures in this paper are available online at <http://ieeexplore.ieee.org>.

Digital Object Identifier 10.1109/TNS.2012.2209893

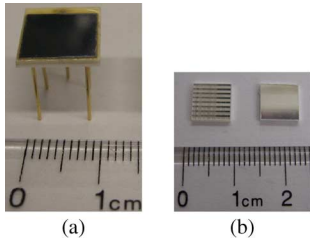


Fig. 1. Photographs of detector components [5], a) PSAPD, b) 8×8 array of 1 mm^3 scintillation crystals.

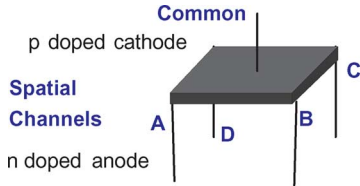


Fig. 2. PSAPD, showing four spatial channels A, B, C, and D.

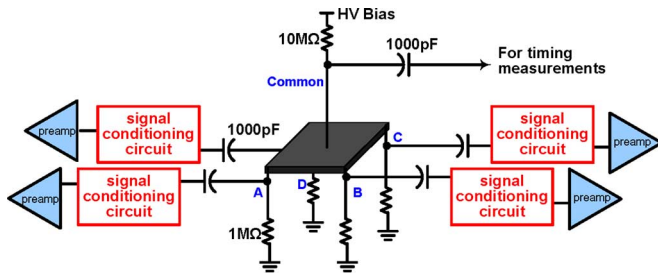


Fig. 3. Connection of PSAPD terminals to biasing, AC coupling and signal conditioning circuitry.

II. METHODS

The signal conditioning circuit was developed for detector modules for a 1 mm^3 resolution Positron Emission Tomography system. The detector modules are comprised of 8×8 arrays of $1 \times 1 \times 1 \text{ mm}^3$ lutetium-yttrium-orthosilicate (LYSO) crystals coupled to $10 \text{ mm} \times 10 \text{ mm}$ PSAPDs fabricated by Radiation Monitoring Devices Inc. (RMD) [1]. The PSAPD and LYSO array are shown in Fig. 1. The $1 \times 1 \times 1 \text{ mm}^3$ crystals are separated by a 3M VM2000 reflector.

Fig. 2 presents a schematic of a PSAPD studied. The PSAPD has four corner contacts, called “spatial channels”, on a high resistivity sheet on the anode for positioning interactions using a position dependent charge splitting. The cathode has a single contact which we call the “common”. The PSAPD is typically biased at 1740 to 1770 Volts and has a breakdown voltage in the range of 1760 to 1790 Volts. Fig. 3 shows the biasing and AC coupling circuitry. The common terminal is connected to a RENA-3 channel which is configured to determine the time of the pulse using a leading edge discriminator [5]. This paper focuses on the spatial channel readout and on analyzing the flood histogram derived from these spatial channels.

The RENA-3 ASIC (from NOVA R&D) [12] was used for readout. The RENA-3 contains 36 channels, where each channel consists of charge-sensitive preamplifier, Gaussian shaper, peak

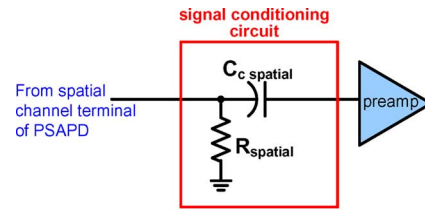


Fig. 4. Signal conditioning scheme.

detect, and sample-hold circuits. Each channel also has a path with a fast shaper and a leading edge discriminator which can be configured to generate a time stamp for the pulses detected.

Each spatial channel of the PSAPD is connected to a RENA-3 channel using the signal conditioning circuit shown in Fig. 4, which essentially high-pass filters the signal, with a cut-off frequency ranging between 3 kHz ($R = 1 \text{ M}\Omega$, $C = 50 \text{ pF}$) and 8 MHz ($R = 5 \text{ k}\Omega$, $C = 4 \text{ pF}$). By varying the values of $C_{c\text{spatial}}$ and $R_{s\text{spatial}}$, we were able to scale the input dynamic range of the signals while controlling the flood histogram crystal identification capability and SNR. For our application, scaling the input dynamic range was necessary in order to prevent saturation of the RENA-3 ASIC since the input dynamic range of the RENA-3 is 54fC whereas the charge from the PSAPD is on the order of 1 pC for a 511 keV annihilation photon assuming a PSAPD gain of 1000.

We implemented the signal conditioning circuit shown in Fig. 4 using a digitally programmable potentiometer (Maxim IC, DS1806E-010) for $R_{s\text{spatial}}$ and a discrete capacitor for $C_{c\text{spatial}}$ which we manually replaced to try different capacitance values. In the future, a programmable capacitor could be used for $C_{c\text{spatial}}$. An Atmel microcontroller (ATmega16a) allowed real-time adjustment of signal conditioning parameters. The detector was flood irradiated with a 30 uCi Na-22 point source 3.5 cm away for 25 minutes to acquire 500,000 counts. All experiments were performed at room temperature (22 degrees Celsius).

In order to increase the statistical power of our results, we computed a global energy histogram to determine the gain and energy resolution of each configuration using the following method which also accounts for per-crystal gain differences. First, the ADC index of the photopeak position (P_i) for each for the 64 crystals in the array was determined by a Gaussian fit ($i = 1 \dots 64$). These photopeak positions vary across the array mainly due to the non-uniform gain of the PSAPD and also due to the non-uniform light yield of the scintillation crystal. Next, the average of these photopeak positions was computed (\bar{P}) and each event assigned to crystal i by the factor (\bar{P}/P_i). That is, the raw data for each crystal i was normalized by multiplying by the factor (\bar{P}/P_i). The data from all the crystals was aggregated together and a histogram was created. To include the effects of x-ray escape, a double-Gaussian was fit to the photopeak, and the FWHM of the Gaussian divided by the mean of the Gaussian is reported as the global energy resolution. The mean of that Gaussian fit is reported as the ADC index of the photopeak which represents the gain.

To analyze the flood histogram quantitatively, the data in the flood image was segmented. First, 64 peaks were identified in

TABLE I
DEFINITION OF FIGURE OF MERIT (FoM) METRICS

	inner FoM	edge FoM
middle rows		
outer rows		

the flood histogram using a peak finding algorithm [13] as implemented in the ROOT data analysis software [14]. We used a minimum distance (L2) norm to assign individual events to crystal locations. A Gaussian was fit to the histogram of the x-coordinates for every crystal for those events with energy within three sigma of the photopeak. The distance between the peaks in the flood histogram and the standard deviation of the peaks are two parameters that measure the crystal identification ability of a given configuration, combined into a Figure of Merit (FoM) metric [5]:

$$FoM = \frac{\text{avg distance between peaks in flood}}{\text{avg width(FWHM) of peaks in flood}} \quad (1)$$

Two separate FoM metrics are calculated since there are systematic differences between the characteristics of the peaks in the inner portion of each row and the edge of each row due to the pin-cushion effect and non-uniform gain across the PSAPD. Table I illustrates how the FoM metrics are calculated. Inner FoM is computed using the inner six peaks in the row, whereas edge FoM is computed using the peak on the left-hand-side edge and the peak on the right-hand-side edge in the row. All the crystals were analyzed, but to condense the results, we only report the FoM for the “middle-rows” and the “outer-rows” using the following definitions illustrated in Table I: FoM for the “middle-rows” is the average FoM for Row 4 and Row 5, and FoM for the “outer-rows” is the average FoM for Row 1 and Row 8.

All studies were performed on two detector modules, Module 0 and Module 1. Table II summarizes the parameters used in the three studies.

Three studies were performed to investigate the influence of the resistor (R_{spatial}) and capacitor (C_{cspatial}) values in the signal conditioning circuit and PSAPD bias voltage on the flood histogram and energy resolution. For Study I, the LYSO array, PSAPD, and signal conditioning circuit was also simulated using the 100 subunit finite element and SPICE model of the PSAPD described in [5]. Each subunit of this PSAPD model

TABLE II
PARAMETERS FOR STUDIES

	R_{spatial} (Ω)	C_{cspatial} (pF)	Bias Voltage (V)
Study I	5k, 10k, 20k, 100k, 1M, infinity (R_{spatial} removed)	fixed to 27	fixed to 1740
Study II	fixed to 10k	4, 10, 18, 27	fixed to 1740
Study III	fixed to 10k	4, 10, 18, 27, 51	1730, 1740, 1750, 1760, 1770, 1780

consists of a 0.45 pF capacitor (since total device capacitance is 45 pF) in parallel with a noise source, connected to the other subunits via resistor elements of 5.2 k Ω to model the sheet resistance at operating bias for the high resistivity layer. The main contributors modeled are shot noise due to 1 μ A of PSAPD leakage current, Poisson variance (assuming 25,000 light photons produced by LYSO per MeV), and thermal noise from the preamplifier. Thermal noise from resistors (e.g., R_{spatial} and bias resistors) is negligible since it is about 100 \times lower than the shot noise of the PSAPD. For each LYSO crystal in the array, the spatial distribution of the light photons produced upon absorption of a 511 keV photon interaction was simulated using Detect 2000. The PSAPD produces charge at the location where the scintillation light hits. Then, the FEM model of the PSAPD, implemented in H-SPICE, determined how the charge is divided by the PSAPD resistive sheet to produce signals at the four corners. One thousand 511 keV photon interactions were simulated. The FEM simulation was repeated for every resistor value. A detailed description of the noise modeling and simulation flow is in [5].

For Study III, an extra dataset with C_{cspatial} set to 51 pF at 1730 V was taken. In Study II, the bias voltage was set to 1740 V, and it was not possible to analyze data when C_{cspatial} was set to 51 pF since the preamplifier was saturated when the bias voltage was 1740 V.

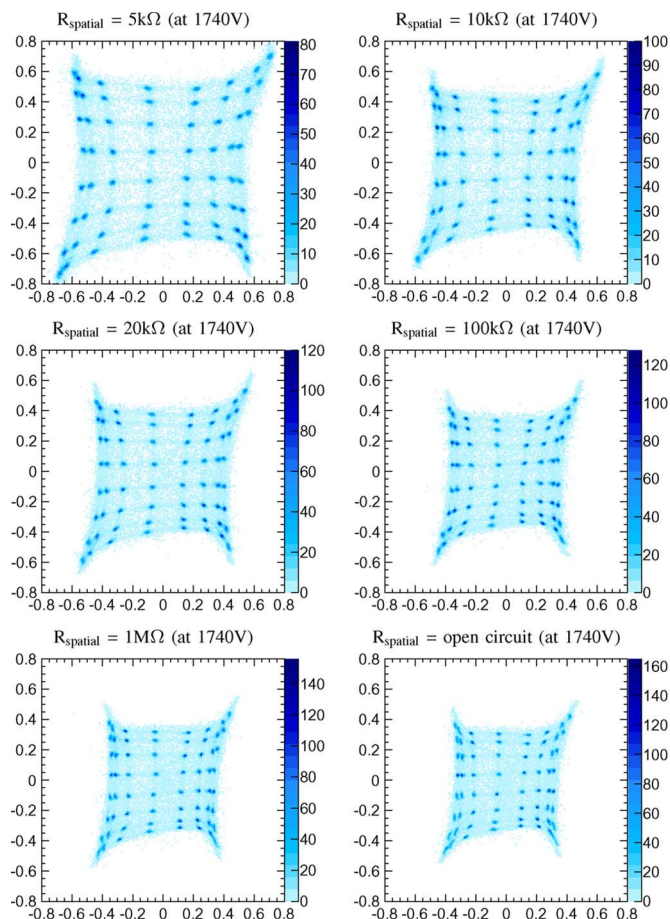


Fig. 5. Study I experimental results: flood histograms for Module 1 for various values of R_{spatial} .

In contrast to the work described in [5] which investigates multiplexing, this paper focuses on the signal conditioning circuit and studies how the parameter values in that circuit affect the flood histogram.

III. RESULTS AND DISCUSSION

A. Study I: Vary R_{spatial}

1) *Experimental Results*: The flood histograms for Module 1 with each R_{spatial} value is shown in Fig. 5. Reducing R_{spatial} causes the spatial dynamic range of the flood histogram to expand, i.e., the x- and y-coordinates fill a larger portion of the range from -1 to 1 . Note that this does not necessarily improve crystal identification, as the width of the peaks also increases. Quantitative results for this study for both Module 0 and 1 are shown in Fig. 6. Fig. 6(a) shows that the attenuation of the signal conditioning circuit increases when smaller R_{spatial} values are used (i.e., the gain, indicated by the ADC index, decreases). Fig. 6(b) shows that there is degradation in energy resolution, and hence SNR, when a low R_{spatial} value of $5 \text{ k}\Omega$ is used. Figs. 6(c) and 6(d) show the Figure of Merit (FoM) results which quantify the flood histogram. The change in FoM when R_{spatial} was varied is within the error bars of the experiment so there is no clear optimal R_{spatial} based on the FoM metric. This also

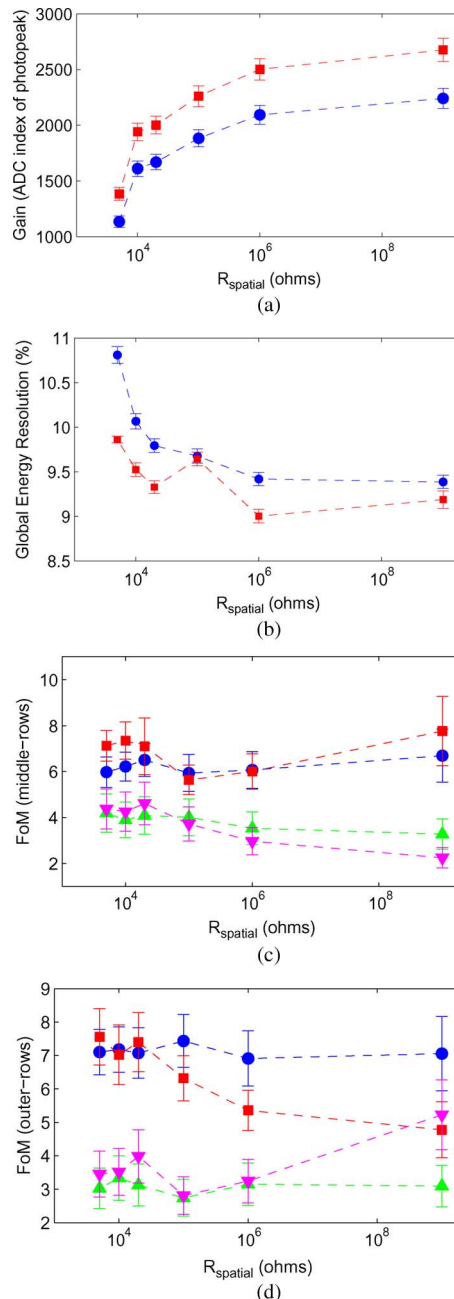


Fig. 6. Study I experimental results: (a) Gain, (b) global energy resolution, (c) FoM of middle-rows, (d) FoM of outer-rows. Error bars represent statistical error (standard error) in the measurement.

implies that the gain can be changed using R_{spatial} without degrading the FoM.

2) *Simulation Results and Analysis*: The results of the flood histogram simulation paralleling the experimental results are depicted in Figs. 7 and 8. In the simulation results, the peaks in the flood histogram appear more well separated and the FoM is higher because intercrystal scatter is not modeled and there may be inaccuracies in the parameters chosen for the noise contributors. Pin-cushion distortion is overestimated due to a number

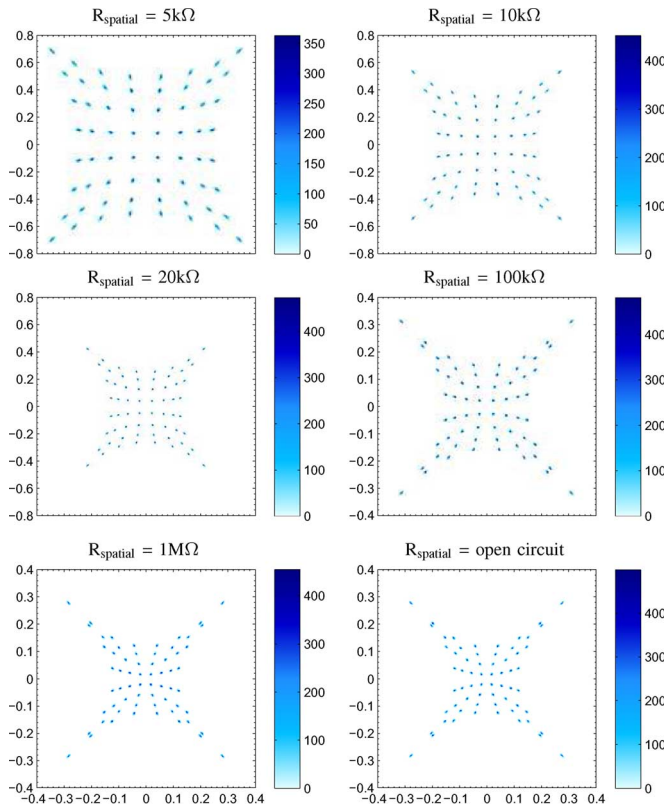


Fig. 7. Study I simulation results: flood histograms for various values of R_{spatial} . Note that the axes were changed for 100 k Ω and above.

of factors not included in the simulation, such as the non-uniform gain of the PSAPD, possible intrinsic non-linearity of the electronics, and error in the estimation of the size and position of contacts on the PSAPD. Therefore, the absolute value of the numbers obtained through the simulation cannot be compared with those obtained through the experiment. However, the trend seen in the simulation can be used to confirm the observation in the experiment that reducing R_{spatial} causes the spatial dynamic range of the flood histogram to expand.

To understand why the spatial dynamic range of the flood histogram changes with R_{spatial} intuitively, we reduce the problem to one dimension and only consider two spatial channels, A and B, as shown in Fig. 9, where the interaction is closer to A. The Anger logic formula for the x-coordinate simplifies as follows:

$$x = \frac{A - B + D - C}{A + B + C + D} \rightarrow x = \frac{A - B}{A + B} = \frac{\frac{A}{B} - 1}{\frac{A}{B} + 1} \quad (2)$$

With a small R_{spatial} that is comparable or less than the PSAPD sheet resistance (5.2 k Ω), the small R_{spatial} dominated over the sheet resistance of the PSAPD, resulting in less sharing of signal between A and B through the sheet resistance, and a larger ratio A/B ($A/B > 1$). From Equation (2), this translates into a larger x-coordinate for this interaction, and therefore a flood histogram with a larger spatial dynamic range. Fig. 10 shows how the ratio A/B changes when R_{spatial} changes.

A small R_{spatial} also resulted in more linear, “square-shaped” flood images since R_{spatial} dominated over the nonlinearity of

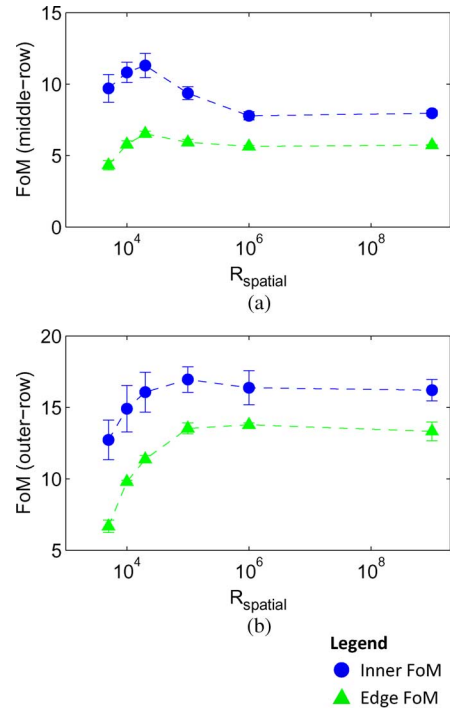


Fig. 8. Study I simulation results: (a) FoM of middle-rows, (b) FoM of outer-rows. Error bars represent statistical error (standard error).

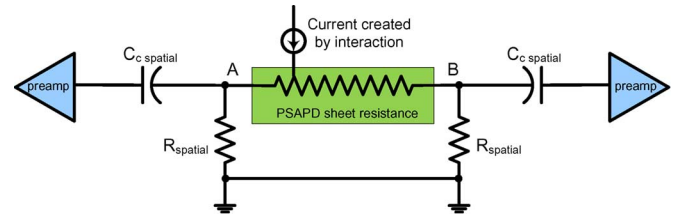


Fig. 9. 1-dimensional simplification of the PSAPD. Interaction closer to spatial channel A than to spatial channel B.

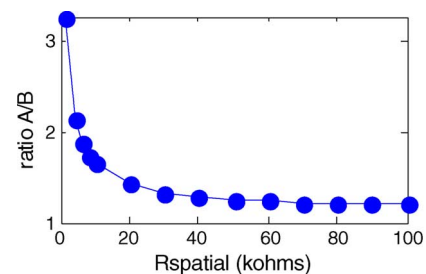


Fig. 10. SPICE simulation of an interaction near the corner for spatial channel A of the PSAPD. R_{spatial} has a significant effect on the ratio between the peak signal at A and B when it approaches the sheet resistance of the PSAPD (5.2 k Ω /square).

the resistive sheet. A more “square-shaped” flood image may facilitate automatic finding and ordering of the peaks using crystal segmentation algorithms [15].

The signal conditioning circuit attenuates the entire output current from the PSAPD (ie, the entire input to the signal conditioning circuit), including both the signal and noise components. So, if all the noise contributors originated from the PSAPD and scintillation crystal, there would be no SNR change. However, the preamplifier is after the signal conditioning circuit,

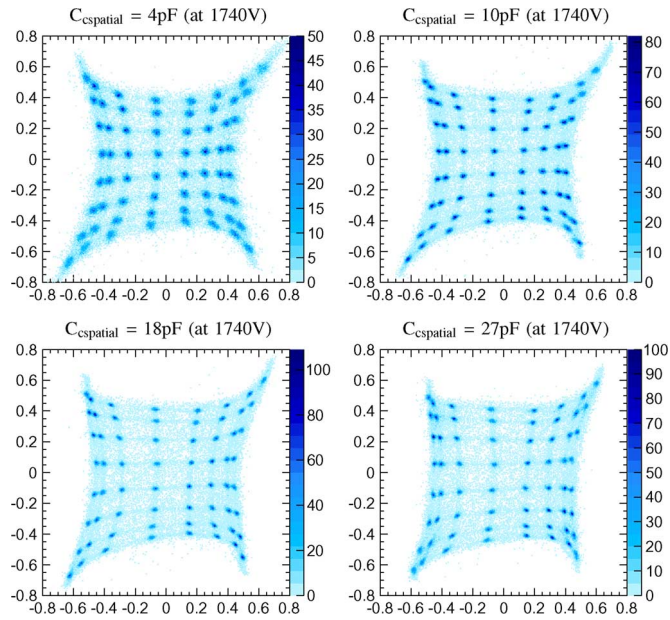


Fig. 11. Study II experimental results: flood histograms for Module 1 at various values of C_{spacial} .

and the preamplifier noise is not affected by the R_{spacial} value to first order, so the SNR degrades. The preamplifier noise is about 16 ADC index units RMS, whereas the signal (the photopeak) ranges from 1100 to 2700 ADC index units as shown in Fig. 6(a). As R_{spacial} was decreased below 10 k Ω , the signal decreased but the preamplifier noise stayed the same so the SNR decreased. This was seen in the simulation. The degradation in the FoM indicated that the increase in the width of the peaks in the flood (which represents noise) was more than the increase in the distance between the peaks (which represents spatial dynamic range expansion). However, this trend could not be clearly seen in the experiment.

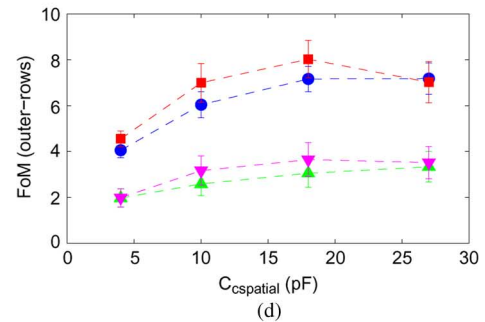
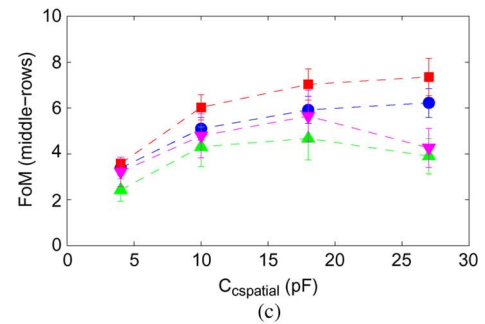
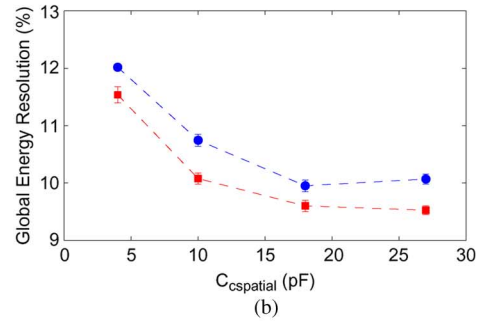
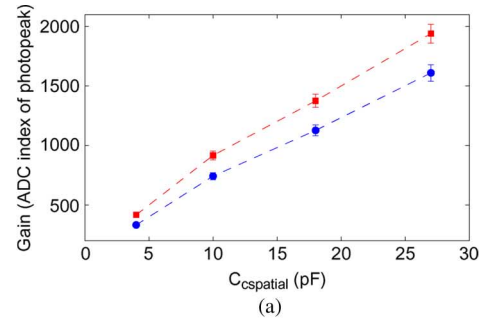
B. Study II: Vary C_{spacial}

The flood histograms for Module 1 with each C_{spacial} value are shown in Fig. 11. The quantitative results for Module 0 and Module 1 are shown in Figs. 12(a) to 12(d). Fig. 12(a) shows that the attenuation of the signal conditioning circuit increases when smaller C_{spacial} values were used (i.e., the gain, indicated by the ADC index, decreases). Fig. 12(b) shows that the energy resolution, and hence SNR, was better for larger C_{spacial} values. Figs. 12(c) and 12(d) shows the Figure of Merit (FoM) results which quantify the flood histograms. FoM was better for larger C_{spacial} values.

C. Study III: Vary C_{spacial} and PSAPD Bias Voltage

Instead of showing the results at all PSAPD bias voltages for each value of C_{spacial} , only the result at the bias voltage that gives the best flood histogram as determined by the average Figure of Merit (“optimal bias voltage”) is presented. Table III lists the bias voltages found to be optimal for each C_{spacial} value.

The flood histograms for Module 1 with each C_{spacial} value are shown in Fig. 13. A visual inspection shows that the quality



Legend for Gain and Energy Resolution Graphs
 ● Module0
 ■ Module1

Legend for FoM Graphs
 ● Module0, Inner FoM
 ■ Module1, Inner FoM
 ▲ Module0, Edge FoM
 ▼ Module1, Edge FoM

Fig. 12. Study II experimental results: (a) Gain, (b) global energy resolution, (c) FoM of middle-rows, (d) FoM of outer-rows. Error bars represent statistical error (standard error) in the measurement.

of the floods are comparable. The quantitative results are in Fig. 14, along with the results for Module 0.

Fig. 14(b) shows a slight improvement in energy resolution as C_{spacial} was increased up to 27 pF. At 51 pF, the energy resolution has degraded. The poor energy resolution at 51 pF is likely because the input-referred noise of the preamplifier increased when the capacitance at its input increased.

TABLE III
OPTIMAL BIAS VOLTAGE FOR EACH MODULE AND EACH C_{cspatial} VALUE

	Module 0	Module 1
4pF	1780V	1780V
10pF	1760V	1750V
18pF	1750V	1740V
27pF	1740V	1730V
51pF	1730V	1730V

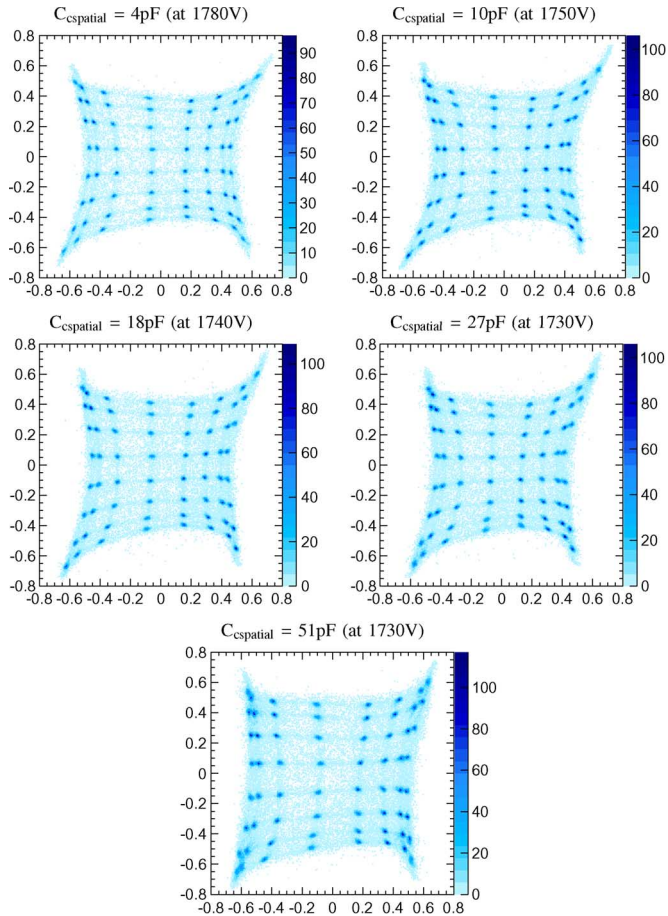
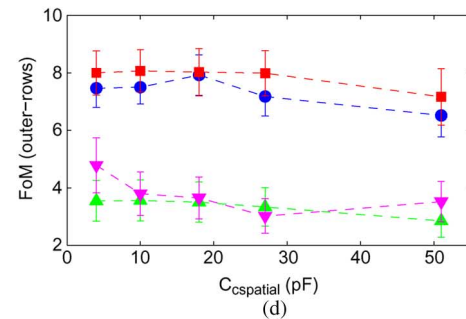
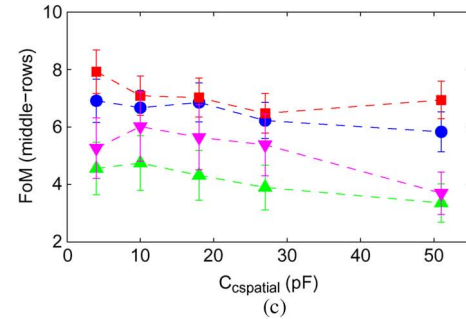
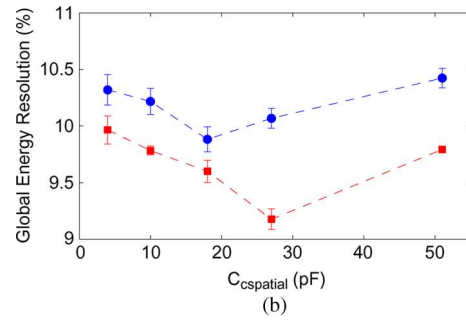
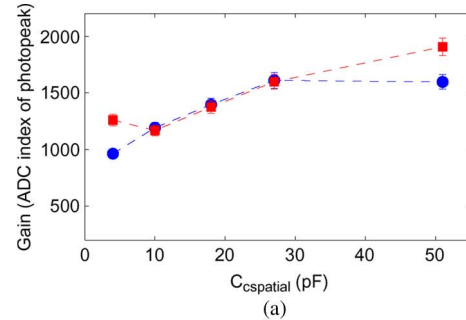


Fig. 13. Study III experimental results: flood histograms for Module 1 at various values of C_{cspatial} at optimal PSAPD bias voltage.

A different bias voltage was used for each data point, and both bias voltage and C_{cspatial} value affect the gain so it is reasonable that we do not see the gain increase with larger C_{cspatial} in Fig. 14(a). It is notable that an ADC index in the range of 1000 to 1600 can be a predictor of a good selection of bias voltage and C_{cspatial} values. This suggests that optimal performance is achieved for similar charge at the RENA input, independent of the PSAPD gain.

Figs. 14(c) and 14(d) show no significant change in FoM for all C_{cspatial} values when the device is at the optimal bias voltage, although there is a minor change in energy resolution. The optimal bias voltage decreases as the C_{cspatial} value increases. Therefore, it can be deduced that for every bias voltage within the range studied (1730 V to 1780 V), there is a C_{cspatial} value that allows the FoM to be maintained. This may be useful in a situation where it is not feasible to have a certain PSAPD



Legend for Gain and Energy Resolution Graphs
 ● Module0
 ● Module1

Legend for FoM Graphs
 ● Module0, Inner FoM
 ■ Module1, Inner FoM
 ▲ Module0, Edge FoM
 ▼ Module1, Edge FoM

Fig. 14. Study III experimental results: (a) Gain, (b) global energy resolution, (c) FoM of middle-rows, (d) FoM of outer-rows. Error bars represent statistical error (standard error) in the measurement.

at its optimal bias voltage since it may be possible to not have degradation in the FoM by setting C_{cspatial} to the value that corresponds to that bias voltage. Further study is needed to fully understand if timing performance would be sacrificed, and how this potential sacrifice compares with the complexity of designing a method to have each PSAPD biased at its optimal bias voltage. However, our results so far [16] indicate that the time resolution only changed from 2.5 to 2.6 ns over a 40 V

bias voltage range. The range of parameters studied in this work was constrained by the limited RENA-3 input dynamic range. Timing information is intended to be readout from the common terminal (see Fig. 3) so the signal conditioning circuit should not directly affect the signal used for timing to first order. However, if there is a second order effect which causes the signal rise time at the common terminal to change (e.g., the circuits are weakly coupled through the detector capacitance), then time resolution may be affected. Further study is needed to confirm the time resolution achievable.

Similarly, changing the signal conditioning parameters to manipulate the dynamic range of the signal may be used to compensate for changes in the detector gain due to temperature changes. Again, further investigation is needed to understand if there is degradation in performance and how the complexity and cost of designing a temperature control system compares with the potential degradation in performance. Future work includes the development of an algorithm that can determine the signal conditioning parameters based on PSAPD gain, PSAPD noise, dynamic range of the electronics, and possibly real-time monitoring of parameters.

IV. CONCLUSION

The flood histogram FoM was not sensitive to the exact value of the resistor in the signal conditioning circuit, but in general, a resistance about twice the sheet resistance on the position sensitive detector was best since this expanded the spatial dynamic range of the flood histogram and reduced the non-linearity of the flood histogram while scaling the signal to fit the electronics input dynamic range. In our setup, the best value for the capacitor in the signal conditioning circuit was 27 pF since it resulted in the best performance taking preamplifier input dynamic range, preamplifier noise, and detector noise into account.

ACKNOWLEDGMENT

The authors thank R. Farrell from RMD for his help.

REFERENCES

- [1] K. S. Shah, R. Farrell, R. Grazioso, E. Harmon, and E. Karplus, "Position-sensitive avalanche photodiodes for gamma-ray imaging," *IEEE Trans. Nucl. Sci.*, vol. 49, no. 4, pp. 1687–1692, 2002.

- [2] J. Zhang, A. M. K. Foudray, P. D. Olcott, R. Farrell, K. S. Shah, and C. S. Levin, "Performance characterization of a novel thin position-sensitive avalanche photodiode for 1 mm resolution positron emission tomography," *IEEE Trans. Nucl. Sci.*, vol. 54, no. 3, pp. 415–421, 2007.
- [3] M. McClish, P. Dokhale, J. Christian, C. Stapels, E. Johnson, R. Robertson, and K. S. Shah, "Performance measurements of CMOS position sensitive solid-state photomultipliers," *IEEE Trans. Nucl. Sci.*, vol. 57, no. 4, pp. 2280–2286, Aug. 2010.
- [4] H. Kume, S. Suzuki, J. Takeuchi, and K. Oba, "Newly developed photomultiplier tubes with position sensitivity capability," *IEEE Trans. Nucl. Sci.*, vol. 32, no. 1, pp. 448–452, Feb. 1985.
- [5] F. W. Y. Lau, A. Vandenbroucke, P. D. Reynolds, P. D. Olcott, M. A. Horowitz, and C. S. Levin, "Analog signal multiplexing for PSAPD-based PET detectors: Simulation and experimental validation," *Phys. Med. Biol.*, vol. 55, no. 23, pp. 7149–7174, Dec. 2010.
- [6] C. Pepin, P. Berard, A. Perrot, C. Pepin, D. Houde, R. Lecomte, C. Melcher, and H. Dauter, "Properties of LYSO and recent LSO scintillators for phoswich PET detectors," *IEEE Trans. Nucl. Sci.*, vol. 51, no. 3, pp. 789–795, June 2004.
- [7] J. Zhang, P. D. Olcott, and C. S. Levin, "A new positioning algorithm for position-sensitive avalanche photodiodes," *IEEE Trans. Nucl. Sci.*, vol. 54, no. 3, pp. 433–437, 2007.
- [8] P. Despres, W. C. Barber, T. Funk, M. McClish, K. S. Shah, and B. Hasegawa, "Modeling and correction of spatial distortion in position-sensitive avalanche photodiodes," *IEEE Trans. Nucl. Sci.*, vol. 54, no. 1, pp. 23–29, 2007.
- [9] Y. Wu, C. Catana, R. Farrell, P. A. Dokhale, K. S. Shah, J. Qi, and S. R. Cherry, "PET performance evaluation of an MR-compatible PET insert," *IEEE Trans. Nucl. Sci.*, vol. 56, no. 3, pp. 574–580, June 2009.
- [10] C. Catana, Y. Wu, M. S. Judenhofer, J. Qi, B. J. Pichler, and S. R. Cherry, "Simultaneous acquisition of multislice PET and MR images: Initial results with a MR-compatible PET scanner," *J. Nucl. Med.*, vol. 47, no. 12, pp. 1968–1976, Dec. 2006.
- [11] S. Kim, M. McClish, F. Alhassen, Y. Seo, K. S. Shah, and R. G. Gould, "Temperature dependent operation of PSAPD-based compact gamma camera for SPECT imaging," *IEEE Trans. Nucl. Sci.*, vol. 58, no. 5, pp. 2169–2174, Oct. 2011.
- [12] T. O. Tumer, V. B. Cajipe, M. Clajus, S. Hayakawa, and A. Volkovskii, "Performance of RENA-3 IC with position-sensitive solid-state detectors," in *Proc. SPIE*, 2008, vol. 7079, p. 70791.
- [13] M. Morh, J. Kliman, V. Matoušek, M. Veselský, and I. Turzo, "Identification of peaks in multidimensional coincidence -ray spectra," *Nucl. Instrum. Methods Phys. Res. A.*, vol. 443, no. 1, pp. 108–125, Mar. 2000.
- [14] R. Brun and F. Rademakers, "ROOT—An object oriented data analysis framework," *Nucl. Instrum. Methods Phys. Res. A.*, vol. 389, no. 1–2, pp. 81–86, Apr. 1997.
- [15] A. Vandenbroucke, A. M. K. Foudray, P. Olcott, and C. S. Levin, "Performance characterization of a new high resolution PET scintillation detector," *Phys. Med. Biol.*, vol. 55, no. 19, pp. 5895–5911, Oct. 2010.
- [16] A. Vandenbroucke, T. J. McLaughlin, and C. S. Levin, "Influence of temperature and bias voltage on the performance of a high resolution PET detector built with position sensitive avalanche photodiodes," *JINST*, vol. 7, no. 8, p. P08001, Aug. 2012.